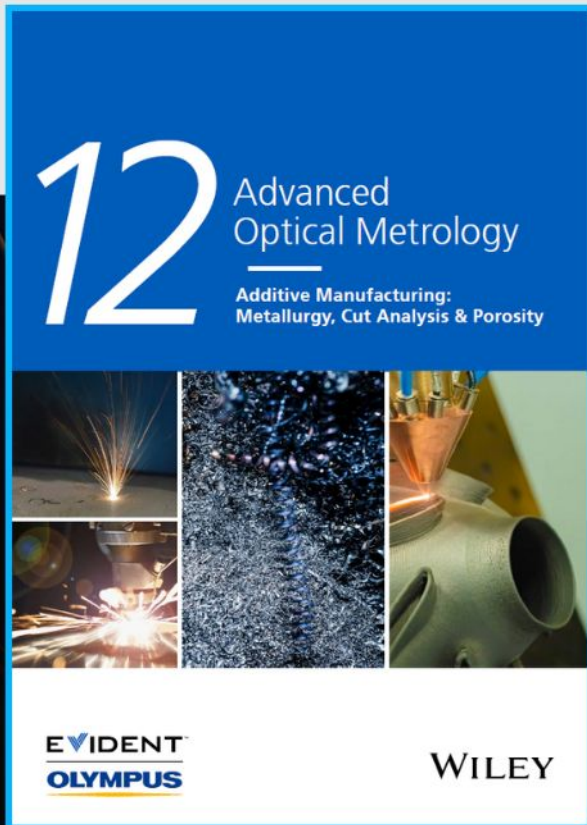




Additive Manufacturing: Metallurgy, Cut Analysis & Porosity



The latest eBook from
Advanced Optical Metrology.
Download for free.

In industry, sector after sector is moving away from conventional production methods to additive manufacturing, a technology that has been recommended for substantial research investment.

Download the latest eBook to read about the applications, trends, opportunities, and challenges around this process, and how it has been adapted to different industrial sectors.

EVIDENT
OLYMPUS

WILEY

Large Spin-to-Charge Conversion at Room Temperature in Extended Epitaxial Sb₂Te₃ Topological Insulator Chemically Grown on Silicon

Emanuele Longo,* Matteo Belli, Mario Alia, Martino Rimoldi, Raimondo Cecchini, Massimo Longo, Claudia Wiemer, Lorenzo Locatelli, Polychronis Tsipas, Athanasios Dimoulas, Gianluca Gubbiotti, Marco Fanciulli, and Roberto Mantovan*


Spin-charge interconversion phenomena at the interface between magnetic materials and topological insulators (TIs) are attracting enormous interest in the research effort toward the development of fast and ultra-low power devices for future information and communication technology. A large spin-to-charge (S2C) conversion efficiency in Au/Co/Au/Sb₂Te₃/Si(111) heterostructures based on Sb₂Te₃ TIs grown by metal–organic chemical vapor deposition on 4" Si(111) substrates is reported. By conducting room temperature spin pumping ferromagnetic resonance, a 250% enhanced charge current due to spin pumping in the Sb₂Te₃-containing system is measured when compared to the reference Au/Co/Au/Si(111). The corresponding inverse Edelstein effect length λ_{IEE} ranges from 0.28 to 0.61 nm, depending on the adopted methodological analysis, with the upper value being so far the largest observed for the second generation of 3D chalcogenide-based TIs. These results open the path toward the use of chemical methods to produce TIs on large area Si substrates and characterized by highly performing S2C conversion, thus marking a milestone toward future technology-transfer.

1. Introduction

Information and Communication Technologies (ICT) are deeply changing our lives and working routines, and this trend got remarkably boosted during the Covid-19 pandemic. In order to improve the overall efficiency and lower the power consumption of any electronic circuit and device, new materials with enhanced functionalities must be brought to a maturity level.

Topological insulators (TIs) represent a state of matter in which the material bulk has insulating properties while the surface hosts highly conducting states.^[1] In TIs, the presence of Dirac-like dispersed surface states jointly with the large spin–orbit coupling (SOC), fixes the electrons spin orientation with respect to their momentum,

E. Longo, M. Belli, M. Alia, M. Rimoldi,^[†] R. Cecchini,^[++] M. Longo,^[+++]
C. Wiemer, L. Locatelli, R. Mantovan
CNR-IMM
Unit of Agrate Brianza (MB)
Via C. Olivetti 2, Agrate Brianza, MB 20864, Italy
E-mail: emanuele.longo@mdm.imm.cnr.it;
roberto.mantovan@mdm.imm.cnr.it

 The ORCID identification number(s) for the author(s) of this article can be found under <https://doi.org/10.1002/adfm.202109361>.

© 2021 The Authors. Advanced Functional Materials published by Wiley-VCH GmbH. This is an open access article under the terms of the Creative Commons Attribution License, which permits use, distribution and reproduction in any medium, provided the original work is properly cited.

^[†]Present address: CERN, European Organization for Nuclear Research, 1211, Geneva 23, Switzerland

^[++]Present address: Consiglio Nazionale delle Ricerche - Istituto per la Microelettronica e Microsistemi (CNR-IMM) Bologna, P. Gobetti 101, Bologna 40129, Italy

^[+++]Present address: CNR-IMM, Unit of Rome, Via Fosso del Cavaliere, 100, Rome 00133, Italy

E. Longo, M. Fanciulli
Università degli studi di Milano-Bicocca
Dipartimento di Scienze dei Materiali
Via R. Cozzi 55, Milano 20126, Italy
P. Tsipas, A. Dimoulas
Institute of Nanoscience and Nanotechnology
National Center for Scientific Research “Demokritos”
Athens 15310, Greece
G. Gubbiotti
Istituto Officina dei Materiali del CNR (CNR-IOM)
Sede Secondaria di Perugia
c/o Dipartimento di Fisica e Geologia
Università di Perugia
Perugia I-06123, Italy

DOI: 10.1002/adfm.202109361

thus generating topologically protected surface states (TSS).^[1] TIs are therefore considered an attracting solution to bring spintronics to the next level in the future ICT,^[2–6] in which the devices functionalities can be driven by a collection of SOC phenomena such as spin Hall effects.^[5] Thanks to their TSS, TIs provide an efficient alternative to the typically used heavy metals (HM) for exploiting spin–charge interconversion effects in heterostructures where TIs and magnetic materials are interfaced.^[6–8] The second generation of 3D-TIs, such as bismuth and antimony chalcogenides-based Bi₂Se₃, Bi₂Te₃, and Sb₂Te₃, is attracting huge interest.^[1,9–11] They are narrow band-gap semiconductors with rhombohedral crystalline structures belonging to the R-3m space group.^[9,11] In principle, exploiting TSS in the second generation of 3D-TIs requires epitaxial quality thin films, a feature that is most commonly achieved by the widely reported molecular beam epitaxy (MBE) deposition method,^[12–16] with several reports about the use of magnetron sputtering also available.^[17–19] In order to fill the gap between research and technology, a firm and decisive effort to develop methods to grow TIs on large-area Si substrates, by simultaneously controlling their functional properties, is highly required. Recently, chemical methods, such as atomic layer deposition, chemical vapor deposition (CVD), and metal–organic CVD (MOCVD) have been shown to allow cost-effective depositions and complex 3D structures on large areas.^[20,21] In a recent review by Zabaveti et al.^[22] a comparison between growth methods for the synthesis of chalcogenides thin films in terms of their lateral dimension has shown the clear advantage in using chemical methods (i.e. cost-effectiveness, complex 3D structures).

We have recently developed a MOCVD process to grow epitaxial-quality Antimony Telluride (Sb₂Te₃) on 4" Si(111) substrates^[21] (Figure S1, Supporting Information). As probed by both angle-resolved photoemission spectroscopy (ARPES) and magnetoconductance (MC) measurements discussed below, when compared to granular-Sb₂Te₃ grown on SiO₂,^[23] the epitaxial-Sb₂Te₃ on top of Si(111) shows improved topological properties especially upon proper annealing, proving clearer and more robust TSS. The next fundamental step is therefore to quantify and optimize spin–charge interconversion phenomena at the interface of the developed TIs with magnetic materials. The use of spin-pumping ferromagnetic resonance (SP-FMR) to investigate spin-to-charge (S2C) conversion at ferromagnets (FM)/HM interfaces has been theoretically described for a long time,^[24,25] and widely demonstrated.^[26–32]

In this work, we report a large S2C conversion occurring at room temperature (RT) in Au/Co/Au/Sb₂Te₃/Si(111) heterostructures, by making use of broadband FMR (BFMR), also known as *all-electrical spin-wave spectroscopy*, and SP-FMR. In the latter experiment, a pure spin current is generated in the Co layer and perpendicularly pumped into the adjacent 3D-Sb₂Te₃, through the Au interlayer, which is found essential for suppressing interfacial non-linear effects due to two magnon scattering (TMS). As a figure of merit for the S2C conversion efficiency quantification, we measure the inverse Edelstein effect length^[33] λ_{IEE} , which is found to range from 0.28 to 0.61 nm. These λ_{IEE} values are comparable or larger than those previously communicated for FM/TIs structures,^[17,26,28,31,32,34] constituting the first report on SP phenomena involving the binary Sb₂Te₃. The successful integration of Sb₂Te₃ on silicon opens interesting routes toward the technology transfer of TIs

for the future of ICT. Finally, by comparing our study with those obtained so far in FM/TIs systems by SP-FMR, we shed light on the influence of the data-treatment to extract λ_{IEE} , pointing toward the need for a unified approach to efficiently compare results from different research groups.^[14]

2. Results and Discussion

2.1. ARPES on Epitaxial Sb₂Te₃

The electronic band structure of the epitaxial Sb₂Te₃ is imaged by ARPES using the 21.22 eV photon excitation energy from a He I plasma source. The in-plane (IP) band dispersion and the constant energy contours (CEC) are shown in **Figure 1**.

A highly dispersive band (red broken line), forming a Dirac-like cone is clearly seen in the inset of Figure 1a. The tip of the Dirac cone is located near the Fermi level E_F or slightly above it, in agreement with previous reports.^[35–37] The Fermi surface and the CEC at a binding energy $E_B = -0.22$ eV in Figure 1b exhibit a characteristic hexagonal shape which is compatible with a 2D-TSS obeying the time-reversal symmetry. This is in clear distinction with a bulk conduction band (BCB), which is expected to be trigonally shaped, reflecting the trigonal symmetry of rhombohedral bulk Sb₂Te₃. It can be inferred from Figure 1a and the Fermi surface in Figure 1b that only the TSS contribute to the Fermi Energy, with no sign of contribution from the BCB, which should exhibit a trigonal symmetry. Moreover, low temperature MC measurements conducted on the Sb₂Te₃ film showed a weak anti-localization effect, a marker of the presence of conductive TSS (Figure S2, Supporting Information). Jointly, ARPES and MC demonstrate the existence of TSS, thus validating the MOCVD-grown epitaxial Sb₂Te₃ thin films as a true TI at RT.

2.2. Effective Spin-Mixing Conductance in Co/Sb₂Te₃ Heterostructures

By BFMR, we measure the evolution of the resonant frequency f_{res} as a function of the resonant magnetic field H_{res} for different Co thicknesses for both the Au(5 nm)/Co(t)/Sb₂Te₃ and Au(5 nm)/Co(t)/Au(5 nm)/Sb₂Te₃ heterostructures. For each Co thickness, the acquired datasets are fitted to the Kittel formula for the uniform magnetization precession in the IP configuration, as described in Figure S5, Supporting Information. Both the sample series show evolution as a function of the Co thickness in accordance with the Kittel formula, similarly to measurements conducted by other groups.^[38,39] This underlines the accurate Co thickness control and the overall high magnetostructural quality of the deposited films. For both the systems, the full width at half maximum (FWHM) of the FMR signals (ΔH^{FWHM}) as a function of the resonant RF frequency (f_{res}) is acquired and reported in Figure S5, Supporting Information. From the latter measurement, the damping constant α of the FM magnetization and the inhomogeneous broadening ΔH_0 are extracted. The ΔH_0 parameter provides information about the magneto-structural quality of the FM film, being fundamental to confirm the reliability of the physical properties obtained by BFMR.^[40] In **Figure 2**, the α values for each sample are extracted as a function of the inverse of the Co thickness ($1/t_{Co}$).

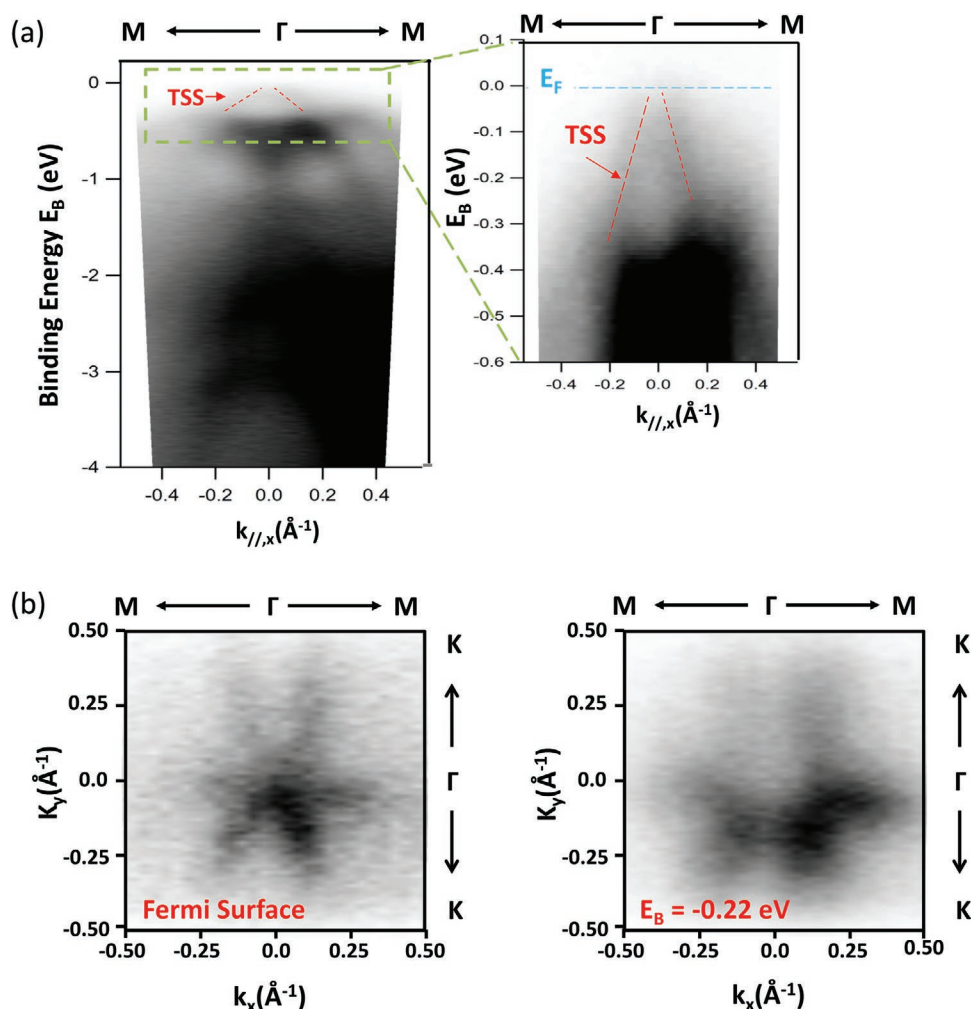


Figure 1. Angle resolved Photoelectron spectroscopy on $\text{Sb}_2\text{Te}_3/\text{Si}(111)$ at RT. a) Energy dispersion as a function of IP wave vector $k_{//,x}$ along the M- Γ -M direction in the first Brillouin zone. TSS denotes the 2D topological surface states forming a Dirac-like cone with the tip just above E_F . The inset shows in magnification the energy range near the Fermi energy E_F . b) CEC at two different binding energies showing the hexagonal symmetry of the TSS bands.

Typically, in the framework of the SP theory,^[25,41] the $\alpha(1/t_{\text{Co}})$ curve follows a linear trend, as described by the first two terms on the right-hand side of Equation (1),

$$\alpha = \alpha_{\text{bulk}} + \text{Re}(g_{\text{eff}}^{\uparrow\downarrow}) \frac{g\mu_B}{4\pi M_s t_{\text{FM}}} + \beta_{\text{TMS}} \frac{1}{t_{\text{FM}}^2} \quad (1)$$

where α_{bulk} represents the damping constant of the bulk material, μ_B the Bohr magneton, M_s the saturation magnetization, g the g factor, t_{FM} the thickness of the FM layer and $\text{Re}(g_{\text{eff}}^{\uparrow\downarrow})$ is the real part of the effective spin-mixing conductance. The latter quantity plays a central role in the description of the SP phenomena, being directly proportional to the spin current density generated in the FM layer and pumped into the adjacent non-magnetic material, here Sb_2Te_3 , at resonance condition.

Clearly, the trend observed for the $\text{Au}(5 \text{ nm})/\text{Co}(t)/\text{Sb}_2\text{Te}_3$ stacks (green stars in Figure 2) does not follow a linear dependence in the whole thickness range. Indeed, by applying the conventional SP fitting model (first two terms in Equation (1)), an $\alpha_{\text{bulk}} = (5 \pm 1) \times 10^{-3}$ is obtained, which is in disagreement with the $(8 \div 11) \times 10^{-3}$ range expected for bulk Co.^[38,42] Being $g_{\text{eff}}^{\uparrow\downarrow}$ a

fundamental parameter to judge spin pumping functionalities, the observed nonlinearity in the $\text{Au}(5 \text{ nm})/\text{Co}(t)/\text{Sb}_2\text{Te}_3$ system must be carefully addressed in order to avoid the extraction of unphysical $g_{\text{eff}}^{\uparrow\downarrow}$ values from BFMR experiments.^[42] The nonlinear α enhancement can origin from magneto-structural disorder in the Co thin films and/or at the $\text{Co}/\text{Sb}_2\text{Te}_3$ interface. Indeed, for the thinnest samples, the obtained inhomogeneous term ΔH_0 shows a slight enhancement when compared to the thicker samples (see Figure S5e,f, Supporting Information). On the other hand, the XRR analysis (Figure S6, Supporting Information) evidences a high chemical-structural quality of the Co layers, suggesting that the divergence observed in Figure 2 for the $\text{Au}/\text{Co}/\text{Sb}_2\text{Te}_3$ set (green stars) likely has other origin.

Actually, L. Zhu et al.^{(2019)^[42]} have recently reported and analyzed the BFMR response in several FM/Pt heterostructures, pointing out that, in the majority of the studied systems, the SP is a relatively minor contribution to α , when measured in the GHz frequency region. Indeed, they suggested that two further terms should be accounted to properly describe the $\alpha(1/t_{\text{Co}})$ curve: spin memory loss (SML) and TMS. SML is an interface effect manifesting with an additional linear contribution

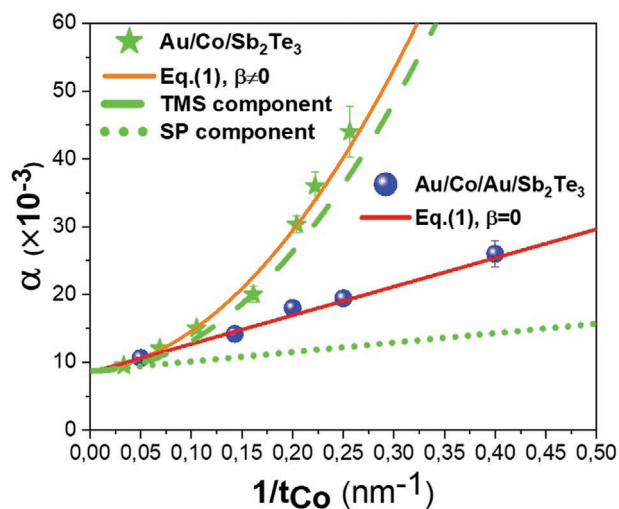


Figure 2. Comparison between the $\alpha(1/t_{Co})$ dispersion for the Au/Co/Sb₂Te₃ (green stars) and Au/Co/Au/Sb₂Te₃ (blue dots) heterostructures. The orange solid line indicates the fit of the collected data for the Au/Co/Sb₂Te₃ stack (green stars) using Equation (1), with β_{TMS} as a free parameter. The dashed and dotted green lines represent the TMS and SP components extracted from the orange solid line fit, respectively. The red solid line indicates the fit of the data for the Au/Co/Au/Sb₂Te₃ structures (blue dots) using Equation (2) where β_{TMS} is null.

to that in Equation (1). Due to SML, the spin current pumped from the precessing magnetization in a FM is partially suppressed at the interface with an adjacent layer, because of back-scattering. Recently, the main source of SML has been attributed to the presence of an abrupt interruption (i.e., at the interface) between a FM and a material with high SOC, such as HM or TIs.^[43] Differently, the TMS is an energy transfer mechanism between the FMR uniform precessional mode and degenerate spin waves.^[44–48] As discussed in Refs. [46,49], the source of the TMS is the presence of defects and imperfections at the surfaces and interfaces of FM thin films, which act as a source of scattering for the precessing magnetization. Indeed, the TMS is often related to the morphological and magnetic roughness at the FM/(HM or TIs) interface. According to Ref. [42], the total damping can be seen as $\alpha = \alpha_{bulk} + \alpha_{SP} + \alpha_{TMS}$, thus giving the full expression in Equation (1), where β_{TMS} is the TMS coefficient, proportional to $\left(\frac{K_s}{M_s}\right)^2$ (with K_s , M_s as the interfacial magnetic anisotropy density and the saturation magnetization, respectively) and to the density of the magnetic defects at the FM/(HM or TIs) interface.^[49] In our system, we cannot separate the linear contributions to $g_{eff}^{\uparrow\downarrow}$ coming from SP or SML, and therefore we consider $g_{eff}^{\uparrow\downarrow}$ as totally originated by SP effects. On the other hand, being the linear region of the green dots in Figure 2 negligible when compared to the parabolic TMS terms, we infer a marginal role played by SML to determine our FMR linewidth. From the global fit of the Au/Co/Sb₂Te₃ data set with Equation (1), we obtain $\alpha_{bulk} = (8.7 \pm 0.9) \times 10^{-3}$, $g_{eff}^{\uparrow\downarrow} = (0.8 \pm 1) \times 10^{19} \text{ m}^{-2}$, and $\beta_{TMS} = (4.5 \pm 0.9) \times 10^{-19} \text{ m}^{-2}$. The α_{bulk} value perfectly agrees with those expected for bulk Co, thus demonstrating how the inclusion of the TMS contribution is necessary to interpret our FMR data set over the whole

range of thicknesses investigated. Therefore, the adopted fitting strategy provides reliable $g_{eff}^{\uparrow\downarrow}$ values, which are comparable to those previously reported in FM/TIs systems (Table 1). In Figure 2, the orange solid line represents the global fit of the Au/Co/Sb₂Te₃ data set (green stars) with Equation (1), where the green dashed and dotted lines are the TMS and SP component, respectively. The observation of the SP component (green dotted line) gives an immediate feeling about how this contribution is almost totally hidden by TMS. The presence of TMS in systems made of FM in contact with non-magnetic materials has been previously investigated by means of angular-dependent FMR measurements.^[47,50,51] On the other hand, we are not aware of similar reports about the use of BFMR to study the influence of TMS at FM/TIs interfaces, thus showing how TMS must be carefully considered in order to extract $g_{eff}^{\uparrow\downarrow}$ values in SP experiments involving TIs, similarly as in FM/HM heterostructures.^[42]

The analysis of the FMR frequency evolution as a function of the applied field by the Kittel formula is reported in Figure S5c,d, Supporting Information, for the set of the Au(5 nm)/Co(*t*)/Au(5 nm)/Sb₂Te₃ samples (*t* = 2.5, 4, 5, 7, 20 nm). The inclusion of the Au interlayer between Co and Sb₂Te₃ totally suppresses the TMS contribution, blue dots in Figure 2, with the $\alpha(1/t_{Co})$ curve now displaying an ideal linear trend. This is directly reflected in lower ΔH_0 values when compared to those extracted for the Au/Co/Sb₂Te₃ stack at similar Co thickness (see Figure S5e,f, Supporting Information). The extracted α values can now genuinely be attributed to SP from Co across the Au(5 nm) interlayer into the epitaxial Sb₂Te₃. Indeed, from the fit of the $\alpha(1/t_{Co})$ data with Equation (2) (now with $\beta_{TMS} = 0$), we obtain $\alpha_{bulk} = (8.5 \pm 0.2) \times 10^{-3}$ and $g_{eff}^{\uparrow\downarrow} = (2.1 \pm 0.1) \times 10^{19} \text{ m}^{-2}$. The extracted α_{bulk} is in perfect agreement with the expected values^[39] thus validating the fitting procedure. The extracted $g_{eff}^{\uparrow\downarrow}$ is well in the $10^{18} - 10^{20} \text{ m}^{-2}$ range reported in most of the FM/(HM, TIs) systems probed by SP-FMR (Table 1, and references therein).

If a FM thin film is in contact with a good spin sink (i.e., HM, TIs), the generation of pure spin currents from FM into HM or TIs is associated with a high $g_{eff}^{\uparrow\downarrow}$ value. In principle, the insertion of an interlayer between FM and the non-magnetic layer, could lead to a reduction of SP depending on the spin diffusion length (λ_s) value characterizing the particular interlayer used.^[52] On the other hand, in the case of TIs, the direct contact with magnetic materials could also have a detrimental effect on the TSS,^[53] which can be otherwise protected with a proper interlayer. Indeed, in FM/(HM, TIs) systems there are several examples where the presence of chemical intermixing and morphological/magnetic interface roughness has been shown to play a key role in the S2C conversion efficiency.^[17,28,29,42,54,55] Therefore, choosing an appropriate interlayer and finding the best trade-off in maintaining the TIs TSS while keeping an efficient spin transport across the FM/interlayer/TIs interface is mandatory but also impressively challenging. By comparing our $g_{eff}^{\uparrow\downarrow}$ with other available results (Table 1), it can be concluded that there is certainly still some room to further enhance the spin mixing at the Co/Au/Sb₂Te₃ interface. A complete overview of different interlayer options to optimize the SP in Co/Sb₂Te₃-based systems is out of the scope of the present paper and may be the subject of future studies.

Table 1. Summary of $g_{eff}^{\uparrow\downarrow}$ and λ_{IEE} values as measured by FMR and SP-FMR (at the indicated temperature T) in stacks with TIs, strained α -Sn and HgTe, and selected HM. The TIs and HMs growth methods are also indicated when available. The reported $g_{eff}^{\uparrow\downarrow}$ values are those obtained following the subtraction of corresponding FMs reference samples. The method to extract λ_{IEE} following Equation (6) (·) or (·-) is also indicated. The data obtained in the present work are reported for comparison. Here, TIs superlattices are not included.^[74]

Stack	Growth of HM or TI	Thickness [nm]	T [K]	$g_{eff}^{\uparrow\downarrow}$ [$\cdot 10^{19} \text{ m}^{-2}$]	λ_{IEE} [nm]	Analysis by Equation (6) [·] or [·-]	REF.
Au/Ni ₈₀ Fe ₂₀	Not reported	20/15	RT	0.9		(·)	[75]
Pt/Ni ₈₀ Fe ₂₀	Not reported	15/15	RT	3.0		(·)	[75]
Pt/Co _{0.2} Ni _{0.8}	Sputtering	6/6	RT	≈2		(·)	[76]
Pt/Co	Sputtering		RT	3.96		(·)	[76]
Pt/Ni _{0.81} Fe _{0.19}	Sputtering	10/10	RT	2.31		(·-)	[59]
Pt/Ni _{0.81} Fe _{0.19}	Sputtering	6/18.5	RT	2.4		(·-)	[60]
(Bi _{0.22} Sb _{0.78}) ₂ Te ₃ /Ni _{0.8} Fe _{0.2}	MBE	6 QL/12	RT	1.0	0.075	(·-)	[69]
Bi ₂ Se ₃ /Ni ₈₁ Fe ₁₉	MBE	20/20	RT	1.5	0.21	(·)	[34]
Sn:Bi ₂ Te ₂ Se/Cu/Ni ₈₁ Fe ₁₉	Bridgman single crystal synthesis	s.c/5/25	40	-	0.10 ± 0.25	(·-)	[77]
α -Sn/Ag/Fe	MBE	30 ML/2/5	RT	7	2.1	(·)	[26]
Ag/Bi	MBE	5–20/8	RT	1.29 ± 3.21	0.2 ± 0.33	(·)	[31]
CdTe/HgTe/Hg _{0.3} Cd _{0.7} Te/NiFe	MBE	200/(10–80)/5/20	RT	-	0.5–2.0	(·)	[78]
Bi ₄₃ Se ₅₇ /Co ₂₀ Fe ₆₀ B ₂₀	Sputtering	2	RT	≈0.7	0.32	(·)	[32]
Bi ₄₃ Se ₅₇ /Co ₂₀ Fe ₆₀ B ₂₀	Sputtering	12	RT	≈0.7	0.10	(·)	[32]
(Bi,Sb) ₂ Te ₃ /Y ₃ Fe ₅ O ₁₂	MBE	6QL/30	RT		0.017 ± 0.035	(·-)	[79]
Tl-Pb/Cu/Ni ₈₀ Fe ₂₀	MBE	2 ML/60/20	15		0.14	(·-)	[71]
Bi ₂ Se ₃ /Bi/Fe	MBE	9QL/Bi(n)/13	RT	≈25 ± 165.7	0.125 ± 0.28	(·)	[80]
Bi ₂ Se ₃ /Y ₃ Fe ₅ O ₁₂	Sputtering	4–16/20	RT	≈0.8–1.36	0.11 ± 0.075	(·)	[17]
(Bi _{0.4} Sb _{0.6}) ₂ Te ₃ /Ni _{0.8} Fe _{0.2}	MBE	9/5	RT	0.9		(·)	[64]
(Bi _{0.4} Sb _{0.6}) ₂ Te ₃ /Te/Ni _{0.8} Fe _{0.2}	MBE	9/4/5	RT	2.36		(·)	[64]
(Bi _{0.4} Sb _{0.6}) ₂ Te ₃ /Al/Ni _{0.8} Fe _{0.2}	MBE	9/3/5	RT	0.08		(·)	[64]
(Bi _{0.4} Sb _{0.6}) ₂ Te ₃ /Al/Ni _{0.8} Fe _{0.2}	MBE	9/6/5	RT	1.71		(·)	[64]
(Bi _{0.4} Sb _{0.6}) ₂ Te ₃ /Ag/Ni _{0.8} Fe _{0.2}	MBE	9/2/5	RT	5.71		(·)	[64]
(Bi _{0.4} Sb _{0.6}) ₂ Te ₃ /Ag/Ni _{0.8} Fe _{0.2}	MBE	9/7/5	RT	2.83		(·)	[64]
Bi ₂ Se ₃ /CoFeB	MBE	5–10QL/5	RT	1.2–26		(·)	[28]
α -Sn/Ag/NiFe	Sputtering	6/2/20	RT	27		(·)	[81]
Sb ₂ Te ₃ /Au/Co/Au	MOCVD	30/5/5/5	RT	0.834	0.28	(·)	This work
Sb ₂ Te ₃ /Au/Co/Au	MOCVD	30/5/5/5	RT	0.6/0.38	0.39/0.61	(·-)	This work

2.3. Spin Pumping in Au/Co/Au/Sb₂Te₃ Heterostructures

In a SP experiment a 3D spin current density J_S^{3D} is generated at resonance in the Co layers, longitudinally injected into Sb₂Te₃ across the Au interlayer, and detected through IP SP-FMR.^[25,31,41,43,56,57] The general expression for J_S^{3D} (in units of A m⁻²) is given by Equation (2).

$$J_S^{3D} = \frac{Re(g_{eff}^{\uparrow\downarrow}) \gamma^2 h_{RF}^2 \hbar}{8\pi\alpha^2} \left(\frac{\mu_0 M_S - \sqrt{(\mu_0 M_S)^2 + 4\omega^2}}{(4\pi M_S \gamma)^2 + 4\omega^2} \right) \frac{2e}{\hbar} \quad (2)$$

where \hbar is the reduced Plank constant, ω the frequency of the RF-signal, e the charge of the electron and h_{RF} the oscillating magnetic field generated by the grounded coplanar waveguide (GCPW).

Following the spin pumping into the Sb₂Te₃ layer, a charge current I_C is generated in the Sb₂Te₃ layer and detected as a potential drop V_{SP} across the measured sample.^[58,59] The electronic transport in our Sb₂Te₃ layers mainly occurs in 2D, as demonstrated by the MC measurements conducted before the Au/Co(/Au) deposition, and interpreted in the framework of the Hikami–Larkin–Nagaoka model (Figure S2, Supporting Information). Therefore, the charge current density J_C^{2D} that is generated by the J_S^{3D} pumping, can be expressed with Equation (3).

$$J_C^{2D} = \frac{V_{SP}}{WR} \quad (3)$$

where W is the width of the sample (Figure 6c in the Experimental Section), R is the sheet resistance as measured separately at four points in the Van der Pauw configuration in the

Table 2. List of samples for the SP-FMR experiments. All the geometrical and electrical quantities used to calculate the S2C conversion efficiency are reported. W indicates the width of each sample, R the sheet resistance, V_{SP} the effective symmetric Lorentzian extracted from the fits (Equation (5)), and J_C^{2D} the corresponding charge current as calculated with Equation (3). As discussed in the main text, the higher α_{S3} value, when compared to α_{S1} and α_{S2} , is due to the lower quality of the Co layer, since no capping layer is employed in S3.

Sample	Stack	α [10^{-3}]	W [mm]	R [Ω]	V_{SP} [μV]	J_C^{2D} [$10^{-3} A m^{-1}$]
S1	Au(5 nm)/Co(5 nm)/Au(5 nm)/Sb ₂ Te ₃ /Si(111)	25.5 ± 0.6	2.46 ± 0.05	14	6.10 ± 0.07	0.178 ± 0.003
S2	Au(5 nm)/Co(5 nm)/Au(5 nm)/Si(111)	20.3 ± 0.2	2.36 ± 0.05	16	1.91 ± 0.04	0.051 ± 0.002
S3	Co(5 nm)/Au(5 nm)/Si(111)	27.6 ± 0.1	2.16 ± 0.05	35	1.26 ± 0.07	0.017 ± 0.002

same setup used for MC studies, and V_{SP} is the voltage that is generated across the sample purely due to the SP from Co into the Sb₂Te₃ layer. The V_{SP} is obtained from the generated transverse mixing voltage V_{mix} , being the quantity directly accessible in a SP-FMR experiment (Figure 6c in the Experimental Section). The first step is therefore to fit the detected V_{mix} with Equation (4).^[60,61]

$$V_{mix} = V_{sym} \frac{\Delta H^2}{\Delta H^2 + (H - H_{res})^2} + V_{asym} \frac{\Delta H(H - H_{res})}{\Delta H^2 + (H - H_{res})^2} \quad (4)$$

where V_{sym} and V_{asym} are the symmetric and anti-symmetric Lorentzian functions, respectively, H_{res} is the value of the magnetic field at the resonance and ΔH is in this case the half-width at half-maximum. From the SP theory,^[24,58,60,62] the symmetric Lorentzian extracted from the fit in Equation (4) can be originated only from the SP contribution to the V_{mix} curve, and ideally $V_{sym} = V_{SP}$. However, this term could also contain the thermal Seebeck effect,^[63] and in order to extract the pure SP contribution, V_{SP} is typically obtained through Equation (5).

$$V_{SP} = \frac{V_{sym}(+H_{ext}) - V_{sym}(-H_{ext})}{2} \quad (5)$$

The so-called “spin rectification terms” contribute to the V_{asym} part, being originated from the anisotropic magnetoresistance and anomalous Hall effect in the Au/Co/Au trilayer.^[58,60–62] The adopted fitting procedure of the SP-FMR data are reported in Figure S7, Supporting Information, for an Au(5 nm)/Co(20 nm)/Au(5 nm)/Sb₂Te₃ stack.

To assess the intrinsic role played by Sb₂Te₃ in boosting the S2C conversion efficiency, the set of samples listed in Table 2 is specifically synthesized. Indeed, to isolate the contribution purely due to Sb₂Te₃ to S2C conversion, the growth of the Au/Co/Au FM stack must be conducted on top of both Sb₂Te₃ and a reference Si(111) substrate simultaneously. This is the only way to quantitatively compare the samples, excluding any potential different aging effect that could take place with and without the Sb₂Te₃. The choice of 5 nm-thick Co layers is motivated by the need to compare with the current literature reporting on S2C interconversion phenomena in TIs-based systems, where the thickness of the FM layer is typically below 10 nm.^[12,14,16,26,32,57,64–66] Moreover, a 5 nm-thick Co layer allows clear signals in both BFMR and SP-FMR configurations, which we compare here, to get a comprehensive picture of the S2C conversion occurring in our systems.

SP-FMR experiments are conducted on all the samples listed in Table 2 by using an RF-power of 132 mW and RF-frequency

of 10.5 GHz. Figure 3a shows the V_{mix} acquired for sample S1 (red dots), together with the FMR signal for the same sample (black triangles), clearly showing the link between the detected V_{mix} and the FMR response of the system. According to the SP theory,^[24] by reversing the direction of the applied magnetic field, the DC voltage relative to the SP contribution must change the sign. This is observed for all the samples in Table 2, with Figure 3b showing the case of sample S1.

Figure 3c summarizes the $(V_{mix} - V_{offset})/WR$ curves for all the samples in Table 2, and the extracted J_C^{2D} values (from Equation (3)) are depicted in Figure 3d and listed in Table 2. As expected, in our measured J_C^{2D} there is a certain contribution from Au, as demonstrated by the different J_C^{2D} detected in S2 and S3. Nevertheless, the presence of Sb₂Te₃ in sample S1 provides a gigantic extra contribution to the S2C conversion, with a 250% enhancement when compared to the reference S2 sample.

The different J_C^{2D} values obtained in samples S2 and S3 indicate that the spin current J_S^{3D} is simultaneously pumped from Co in both the Au layers. Thus, most likely, in sample S1 the spin current pumped into the Au capping layer is reflected at the Au/air interface and then partially absorbed by the Sb₂Te₃ substrate. Considering that λ_S for Co and Au is ≈ 10 and ≈ 35 nm, respectively,^[58,67] a tentative sketch of the J_S^{3D} scheme in S1, S2, and S3 is depicted in Figure 4. Here, the J_S^{3D} backflows at the Au/Sb₂Te₃ and Au/Si(111) interfaces, are not considered.

In the case of sample S3, the larger ΔH_{S3} (175 ± 3 Oe) when compared to both S1 (86.5 ± 0.8 Oe) and S2 (75.5 ± 2.6 Oe), is attributed to the partial Co oxidation due to air exposure. This induces additional structural and magnetic disorder that reflects into a higher magnetic damping.

2.4. S2C Conversion Efficiency in Au/Co/Au/Sb₂Te₃ Stacks

Our main interest is now to translate the observed additional giant 250% increase in the SP contribution due to Sb₂Te₃ (Figure 3d and Table 2), into S2C conversion efficiency. Univocally separating the contribution to V_{SP} arising from bulk inverse spin–Hall effect (ISHE)^[68] and interface IEE is challenging. On the other hand, the simultaneous occurrence of the following experimental evidences: i) successful SP-FMR signal only measured when an Au interlayer is employed (see Figure 3 and Figure S9, Supporting Information); ii) ARPES detection of TSS at the surface of Sb₂Te₃ at RT; iii) 2D-transport in Sb₂Te₃ demonstrated by MC measurements (Figure S2, Supporting Information), strongly supports the S2C as intimately occurring through the TSS, with the IEE being therefore the

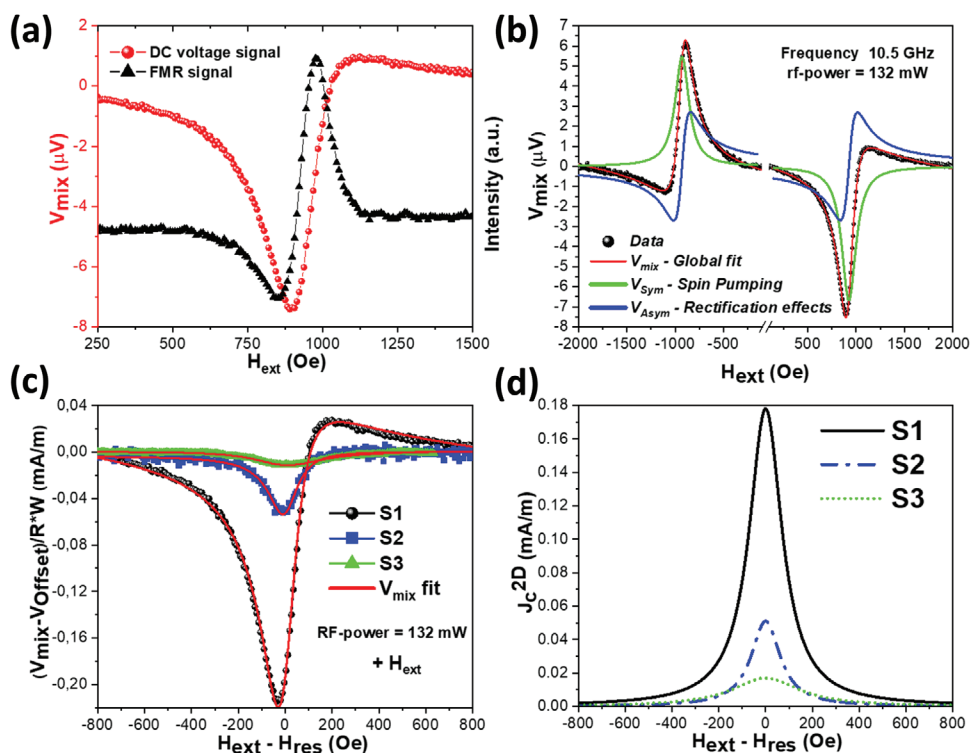


Figure 3. a) SP DC voltage signal for sample S1 acquired at $f = 10.5$ GHz (red circles). The FMR signal at the same resonance frequency is acquired (black triangles), showing the match between the two signals. b) The same SP measurement reported in (a) is performed also for negative values of the external magnetic field. Here, it is evident as the asymmetric component V_{asym} does not depend on the sign of the magnetic field, which is typical for rectification effects due to AMR and AHE. On the other hand, the symmetric component V_{sym} changes sign upon magnetic field reversal, indicating a magnetic-field dependent spin accumulation. The latter condition is in accordance with SP effects. c) $V_{\text{mix}} - V_{\text{offset}}$ signal acquired for samples S1 (black dots), S2 (blue squares), and S3 (green triangles), normalized to the R and W values for each sample. d) 2D charge current density ($J_{\text{c}}^{2\text{D}}$) extracted from the V_{sym} component of the V_{mix} signals reported in (a) and calculated using Equations (3) and (5).

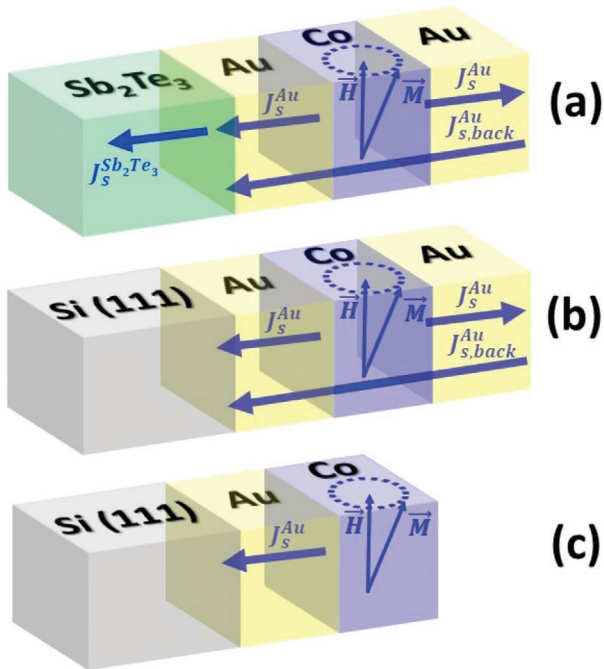


Figure 4. Pictorial view of the generated $J_{\text{c}}^{3\text{D}}$ current flows in the a) S1, b) S2, and c) S3 samples during the conducted SP-FMR experiments.

dominating conversion process.^[33] An alternative interpretation of the S2C conversion in terms of ISHE is given in the Supporting Information. Within IEE, the conversion figure of merit is $\lambda_{\text{IEE}} = J_{\text{c}}^{2\text{D}} / J_{\text{s}}^{3\text{D}}$.^[26,32,69]

In order to extract the pure contribution due to the Sb_2Te_3 , the $g_{\text{eff}}^{\uparrow\downarrow}$ required to calculate $J_{\text{s}}^{3\text{D}}$ through Equation (2), must be obtained by considering the additional damping observed in S1 when compared to the reference S2, that is, the additional contribution purely originating from the presence of Sb_2Te_3 .^[57] This can be done by either considering the difference of the sample damping parameters $\alpha_{\text{S1}} - \alpha_{\text{S2}}$ (Equation (6)(\cdot))^[32,70] or the linewidth of their SP-FMR signals ($\Delta H_{\text{S1}} - \Delta H_{\text{S2}}$) (Equation (6)($\cdot\cdot$)).^[28,58,69]

$$\begin{aligned} g_{\text{eff},\text{Sb}_2\text{Te}_3}^{\uparrow\downarrow} &\doteq \frac{4\pi M_{\text{s}} t_{\text{FM}}}{g\mu_{\text{B}}} (\alpha_{\text{S1}} - \alpha_{\text{S2}}) \\ &\doteq \frac{2M_{\text{s}} t_{\text{FM}} \gamma}{g\mu_{\text{B}} f} (\Delta H_{\text{S1}} - \Delta H_{\text{S2}}) \end{aligned} \quad (6)$$

In our opinion, the first approach (Equation (6)(\cdot)) is the most accurate since α can be obtained from a linear fit of the FMR broadening change as a function of the resonance frequency, while the second approach (Equation (6)($\cdot\cdot$)) only considers the difference of the FMR signal broadening

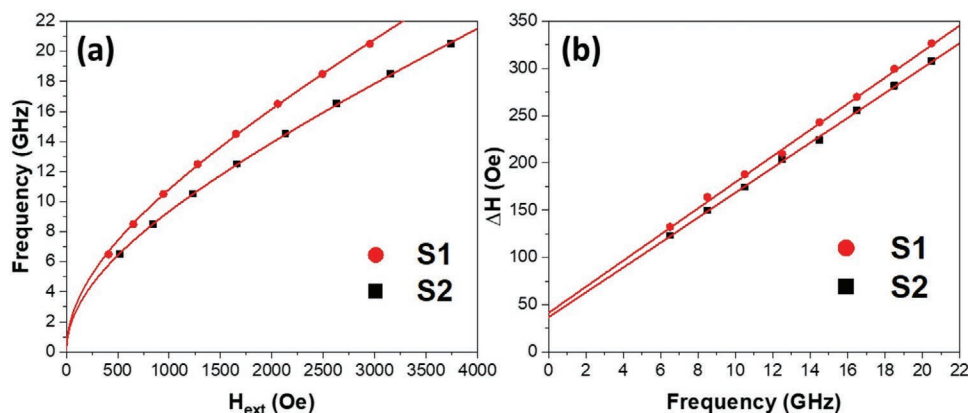


Figure 5. BFMR data for samples S1 (red circles) and S2 (black squares). In a) f_{res} is reported as a function of the resonant magnetic field. From the Kittel fit (red solid line) the g -factor and M_{eff} values are extracted for the two samples and reported in the text. b) The BFMR signal linewidth for samples S1 and S2 is shown as a function of the resonant frequency (f_{res}). Here, the damping constants (α) and the inhomogeneous broadening (ΔH_0) are extracted from the linear fit (red solid line) and the values reported in the text.

at a fixed frequency. On the other hand, the latter strategy is still at the basis of several reports about SP efficiency in FM/(HM, TIs) systems.^[28,59,60,69,71] In fact, the FMR measurements have been typically conducted by adapting cavity electron paramagnetic resonance facilities, with a single RF excitation frequency.^[40] It is also not uncommon to see reports of S2C efficiencies extracted from samples having a single FM thickness, and measurements based on a single frequency.^[70,71]

In the following, we extract λ_{IEE} with both approaches. **Figure 5a** shows the evolution of the $f_{\text{res}}(H_{\text{res}})$ curves measured in S1 and S2 and fitted with the Kittel equation for the IP configuration, from which we obtain: $M_{\text{eff}}^{\text{S1}} = 603 \pm 46 \frac{\text{emu}}{\text{cm}^3}$, $g^{\text{S1}} = 2.64 \pm 0.08$, $M_{\text{eff}}^{\text{S2}} = 653 \pm 29 \frac{\text{emu}}{\text{cm}^3}$, $g^{\text{S2}} = 2.20 \pm 0.04$.

From the linear best-fit of the FMR signal linewidth as a function of the resonant frequency reported in **Figure 5b**, $\alpha_{\text{S1}} = (25.5 \pm 0.6) \times 10^{-3}$ and $\alpha_{\text{S2}} = (20.3 \pm 0.2) \times 10^{-3}$ are extracted. According to Equation (6)(·), these values give $g_{\text{eff}, \text{Sb}_2\text{Te}_3}^{\uparrow\downarrow} = 8.34 \times 10^{18} \text{ m}^{-2}$, which from Equation (2) provides $J_S^{3\text{D-Sb}_2\text{Te}_3} = 6.4 \times 10^5 \text{ A m}^{-2}$ as the pure accumulation due to the presence of Sb_2Te_3 in S1. By considering the J_C^{D} measured for S1 (Table 2), a $\lambda_{\text{IEE}} \approx 0.28 \text{ nm}$ value is finally calculated. We now follow the methodology expressed in Equation (6)(··). In particular, we consider the $\Delta H_{\text{S1}} - \Delta H_{\text{S2}} = 11 \text{ Oe}$ value extracted from the SP experiment at the chosen frequency of 10.5 GHz, which provides a $g_{\text{eff}, \text{Sb}_2\text{Te}_3}^{\uparrow\downarrow} = 6 \times 10^{18} \text{ m}^{-2}$ (Equation (6)(··)) and, from Equation (2), $J_S^{3\text{D-Sb}_2\text{Te}_3} = 4.6 \times 10^5 \text{ A m}^{-2}$, finally resulting in $\lambda_{\text{IEE}} \approx 0.39 \text{ nm}$. However, if this single frequency approach described by Equation (6)(··) is applied for the FMR signal for the same fixed RF frequency of 10.5 GHz and considering the ΔH^{FWM} as the correct value for the FMR signal linewidth, $g_{\text{eff}, \text{Sb}_2\text{Te}_3}^{\uparrow\downarrow} = 3.8 \times 10^{18} \text{ m}^{-2}$ and $J_S^{3\text{D-Sb}_2\text{Te}_3} = 2.9 \times 10^5 \text{ A m}^{-2}$ are extracted. From the latter values $\lambda_{\text{IEE}} \approx 0.61 \text{ nm}$ is then calculated.

The difference in the obtained λ_{IEE} values by following the approaches of Equation (6)(·) and (··), is relevant (Table 1). This difference underlines the importance of establishing a common way of reporting S2C conversion efficiencies as measured through SP-FMR. In fact, this represents a necessary step

to reliably compare similar FM/(HM, TIs) systems. Moreover, the fitting procedure of the SP-FMR data is not the only controversial aspect that strongly influences the S2C efficiency estimation. As previously pointed out, the FMR signal can be affected by a relevant inhomogeneous broadening contribution, for instance, due to magneto-structural disorder^[30] (i.e., magnetic dead layers, presence of different polymorphs in the same FM layer, magnetic roughness) or due to the presence of TMS,^[42] revealing that the FMR signal linewidth is not always reflected in an effective SP response. As it follows from Equation (6), this aspect is directly involved in the calculation of $J_S^{3\text{D}}$. Commonly, the subtraction of a proper reference is the only adopted method, and thus considered effective in eliminating all the spurious contributions to the linewidth broadening. Nevertheless, some of us have demonstrated that the substrate selection has an important role in governing the magneto-structural properties of a FM thin film, suggesting that unwanted inhomogeneous contributions to the linewidth can be overlooked.^[72] In our system, the Co layer is deposited simultaneously on top of the Au interlayer in both the S1 and S2 samples and the XRR measurements show a high-quality Au/ Sb_2Te_3 interface (Figure S6, Supporting Information). In our opinion, these aspects are a reliable strategy to validate the use of the reference subtraction method to extract S2C efficiency. Also based on the latter considerations, as recently reported by Nakahashi et al., a more direct and affordable strategy is to measure the $\Delta H(f_{\text{res}})$ curve evolution directly from the SP signal.^[73]

Table 1 reports a collection of relevant $g_{\text{eff}}^{\uparrow\downarrow}$ and λ_{IEE} data as obtained by FMR-based methods for heterostructures including the second generation of chalcogenide-based 3D-TIs, strained α -Sn and HgTe, and a selection of HM. The different methods used to interpret the FMR data (Equation (6)(·) versus (··)) are also indicated, with the aim to highlight the need of a standardized procedure of data reporting.

If we consider the RT λ_{IEE} value extracted with the single-frequency approach, the measured $\lambda_{\text{IEE}} \approx 0.61 \text{ nm}$ value is, to our knowledge, higher than any other reported S2C conversion efficiency in the second generation of chalcogenide-based TIs (i.e., Bi_2Se_3 , Bi_2Te_3 , and Sb_2Te_3), and lower only than those reported for the strained TIs α -Sn^[26] and HgTe^[78] (Table 1). The

lower limit $\lambda_{IEE} \approx 0.28 \text{ nm}$ is at least of the same order of magnitude (and often higher) of those observed in 3D-TIs produced by MBE or sputtering (Table 1), thus proving the suitability of MOCVD to produce high performing TIs on large-area Si substrate. When compared to the higher S2C efficiency reported for α -Sn^[26] and HgTe,^[78] we underline that the appearance of TSS in the second generation of 3D-TIs, such as Sb₂Te₃, do not require strain engineering, thus allowing their integration on silicon-based technologies. According to the obtained λ_{IEE} values, the system here presented may be of interest in the development of magnetoelectric spin-orbit logic devices.^[82]

The key to understanding the origin of this very large S2C efficiency may lie in the structure and morphology of our Sb₂Te₃ layers grown by MOCVD. Recent works have discussed the influence of grain size and grain boundaries in the S2C conversion in Bi₂Se₃-based heterostructures as probed by SP-FMR.^[17,32,69,83] Interestingly, the granular Bi₂Se₃ has been shown to be more efficient in terms of S2C conversion, with a λ_{IEE} being three times higher than in crystalline Bi₂Se₃.^[17] As shown by transmission electron microscopy, even though our optimized Sb₂Te₃ layers develop an epitaxial nature character, several grain boundaries are still present.^[21] In particular, our films are highly ordered and made by compact Sb₂Te₃ crystalline grains with an average diameter that can be estimated between 15 and 20 nm, see Figure S8, Supporting Information. These grain boundaries may locally influence either the $J_s^{3D} \rightarrow J_c^{2D}$ conversion (i.e., SP) and the subsequent longitudinal transport through the TSS. According to Ref. [17], this may be a possible origin of the observed large λ_{IEE} . This fundamental aspect could be investigated by studying λ_{IEE} for different Sb₂Te₃ thicknesses, even if the tuning of the Sb₂Te₃ thickness through the developed MOCVD process is not straightforward.

Certainly, there is a fundamental role played by the Au interlayer in the observed large λ_{IEE} (see Figure S9, Supporting Information). Several groups have already tried to decouple the FM/TIs interface by introducing an interlayer. For instance, in the seminal work of Rojas-Sanchez et al. (2016)^[26] the introduction of an Ag interlayer in the Au/Fe/Ag/ α -Sn structure has been proven to effectively enhance the S2C efficiency by reaching $\lambda_{IEE} = 2.1 \text{ nm}$, as extracted from SP measurements at RT. More recently, the thorough study of the S2C conversion efficiency on the spin-orbit torque response in different Py/Interlayer/(Bi,Sb)₂Te₃ systems has been reported by F. Bonell et al.^[64] where the introduction of different metallic spacers (i.e., Te, Ag, Al) has been proven as effective in largely enhancing the S2C efficiency as due to the suppression of the interface intermixing and band-bending. Specifically, by following an accurate chemical-structural description of the Py/Interlayer/(Bi,Sb)₂Te₃ interfaces, they have evidenced criticalities concerning the Te out-diffusion from (Bi,Sb)₂Te₃. In our previous works,^[84,85] we have reported very similar arguments for what concerns the Te interdiffusion in Fe/Sb₂Te₃ heterostructures, where a “FeTe” type of bonding at the interface is highly favored. Being FeTe a paramagnetic compound, it could hinder any S2C conversion effect at the interface, or at least largely limit the efficiency of such conversion. As a matter of fact, this is one of the main motivations for our choice of a 5 nm Au buffer layer at the Co/Sb₂Te₃ interface. The Au interlayer efficiently suppresses

several detrimental effects at the Co/Sb₂Te₃ interface, the main one being certainly the TMS (Figure 2).

The transport properties of the TSS for several free-standing TIs can be studied by different techniques such as ARPES and scanning tunnel microscopy (STM).^[26,86] According to the calculation carried out by Fert and Zhang in Ref. [87], the λ_{IEE} can be written as the product $\lambda_{IEE} \equiv v_f \tau_p$, where v_f is the Fermi velocity and τ_p is the momentum relaxation time, which accounts for the electronic scattering in the TIs bands. The λ_{IEE} can be considered as equivalent to the longitudinal mean free path at the metal-TIs interface. The obtained $\lambda_{IEE} \approx 0.61 \text{ nm}$ can be regarded as the upper limit for the electronic ballistic transport across the Au/Sb₂Te₃ interface. This value is lower than those reported for free-standing Sb₂Te₃ surfaces, where several tens of nanometers have been reported (as in Ref. [86]). In the latter work, a Fermi velocity of $v_f \approx 4.3 \times 10^5 \text{ ms}^{-1}$ has been extracted for the TSS of a crystalline Sb₂Te₃ thin film, as measured by STM measurements. Assuming $\lambda_{IEE} \approx 0.61 \text{ nm}$, we can extract $\tau_p \approx 1.7 \text{ fs}$. On the other hand, the presence of the additional Au layer in contact with Sb₂Te₃, could introduce additional relaxation mechanisms for the Sb₂Te₃ TSS, which can be at the origin of the discrepancy between the mean free path in the Sb₂Te₃ layer, when measured through STM or SP-FMR. As suggested in Refs. [26,64], the use of an insulating interlayer in place of a metallic one could solve this problem, preserving more efficiently the TSS and consequently further improving the λ_{IEE} value. However, the use of an insulating layer as a spacer between the FM and the TI layers to preserve the TSS still represents an open issue. Indeed, for instance, in Ref. [32], a 2 nm MgO interlayer has been used to demonstrate the suppression of the SP pumping signal, as compared to the same system without interlayer.

3. Conclusion

RT SP-FMR is successfully employed to measure the S2C conversion occurring in the large-area Sb₂Te₃ TI produced by MOCVD on 4" Si(111) wafers. An inverse Edelstein Effect length λ_{IEE} from 0.28 up to 0.61 nm has been measured, and the two values being the outcome of commonly used different methodological analysis. Even the lower observed value is at least comparable (and often larger) than those previously reported in chalcogenide-based 3D-TIs produced by sputtering or MBE. Our results constitute a “year zero” for the use of chemical methods to fabricate TIs for highly efficient S2C converters, providing a milestone toward the future realistic technology-transfer. To our knowledge, this is also the first report of spin pumping in the binary Sb₂Te₃. A further improvement of the observed S2C conversion performances could be achieved by manipulating the Fermi level with appropriate material engineering.^[14] Our results also point out the need to standardize the reporting of S2C conversion efficiency as probed by SP-FMR. While our manuscript was under review a paper reporting SP-FMR in Sb₂Te₃ grown by MBE has been published, with a measured λ_{IEE} of about 0.28 nm,^[88] in perfect agreement with our results.

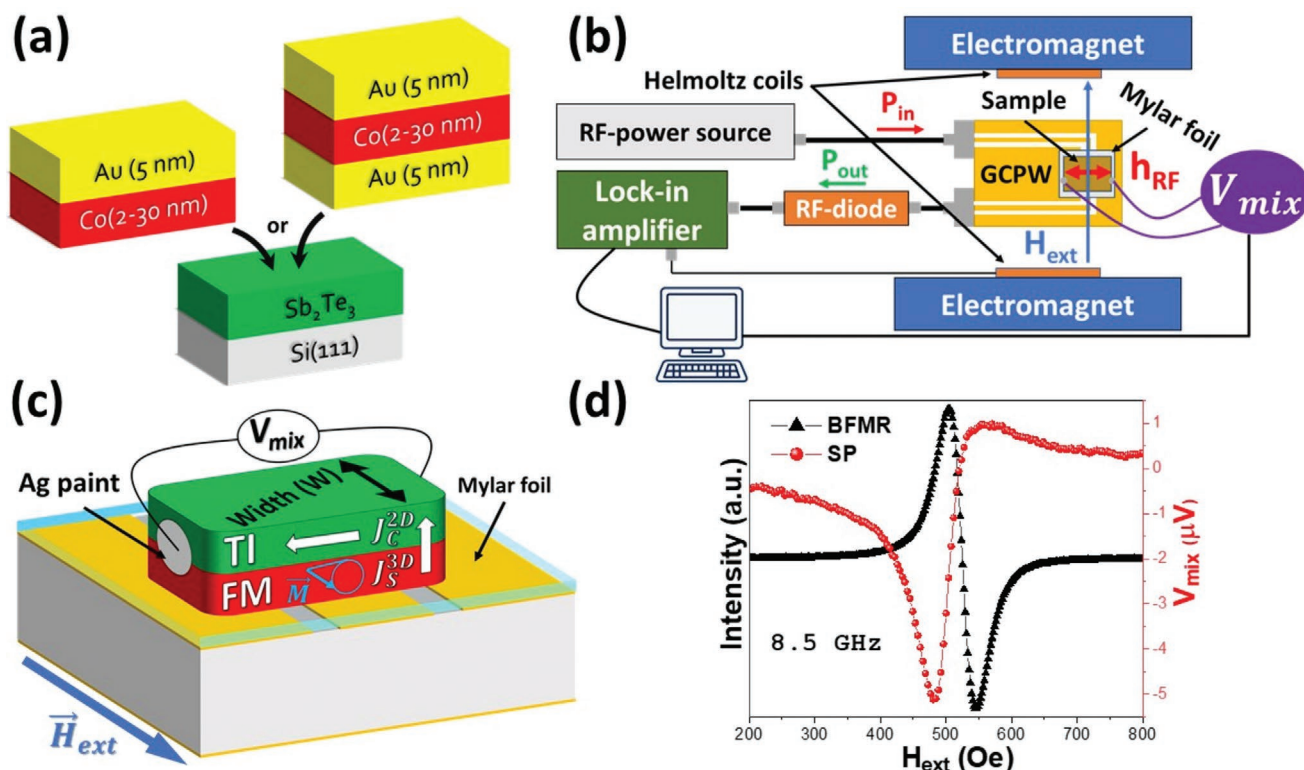


Figure 6. a) Stacking of the investigated heterostructures. b) BFMR and SP-FMR experimental setup. c) The geometrical configuration of the sample (width: W) when mounted flip-chip on the GCPW and electrically connected to a nano-voltmeter through Ag wires and Ag paint. The DC-voltage signal (V_{mix}) is collected at the sample boundaries. d) Examples of the acquired FMR (black triangles) and SP-FMR (red dots) signals for Au(5 nm)/Co(20 nm)/Au(5 nm)/Sb₂Te₃ heterostructures at the fixed RF frequency of 8.5 GHz and fixed RF power of 73 mW. The superposition of the curves demonstrates the direct connection between the two physical phenomena.

4. Experimental Section

Sb₂Te₃ thin films with a nominal thickness of 30 nm were deposited at RT by MOCVD on 4" intrinsic Si(111) wafers (resistivity > 10 000 Ω cm) exploiting an AIXTRON 200/4 system, operating with an ultra-high pure Nitrogen carrier gas and equipped with a cold wall horizontal deposition chamber accommodating a 4" IR-heated graphite susceptor (Figure S1, Supporting Information). In order to promote an epitaxial order, the Sb₂Te₃ films were subjected to specific in situ thermal treatments.^[21]

The Au(5 nm)/Co and Au(5 nm)/Co/Au(5 nm) capping layers were prepared by e-beam evaporation on pre-cut $\approx 1 \times 1$ cm² Sb₂Te₃ pieces using an Edwards Auto306 facility, producing Au(5 nm)/Co(t)/Sb₂Te₃ and Au(5 nm)/Co(t)/Au(5 nm)/Sb₂Te₃ heterostructures, with the nominal thickness (t) within the 2–30 nm range (Figure 6a).

The BFMR and SP-FMR experiments were conducted using a homemade setup as depicted in Figure 6b, where the sample was positioned between the polar extensions of a Bruker ER-200 electromagnet, maintaining its surface parallel to the external magnetic field (H_{ext}) in the so-called “flip-chip” configuration for IP measurements.^[89] To induce an oscillating magnetic field in the FM layer, the sample was fixed on a custom GCPW (Figure 6b,c) connected to a broadband Anritsu RF-source (Figures S3 and S4, Supporting Information). The FMR signal for a fixed RF frequency was performed by measuring the derivative of the absorption power downstream of the electrical transmission line as a function of H_{ext} through a lock-in amplifier (Figure 6b). In the SP-FMR experimental configuration, the sample edges were connected to a nano-voltmeter with Ag wires soldered with Ag paint and a voltage signal (V_{mix}) was measured as a function of H_{ext} (Figure 6c). In Figure 6d, an example of the FMR (black triangles) and SP-FMR (red dots) signals detection as recorded in an Au(5 nm)/

Co(20 nm)/Au(5 nm)/Sb₂Te₃ sample at 8.5 GHz, is reported. The two signals were revealed simultaneously and resonated perfectly at the same external magnetic field, demonstrating the correlation between the occurring physical effects.

Supporting Information

Supporting Information is available from the Wiley Online Library or from the author.

Acknowledgements

The authors acknowledge funding from the European Union's Horizon 2020 project SKYTOP “Skyrmion-Topological Insulator and Weyl Semimetal Technology” (FETPROACT 2018-01, no. 824123).

Open access funding provided by Consiglio Nazionale delle Ricerche within the CRUI-CARE Agreement.

Conflict of Interest

The authors declare no conflict of interest.

Author Contribution

E.L. and M.B. developed the BFMR and SP-FMR set-up. E.L. conducted all the BFMR, SP-FMR, and XRR measurements, and performed the analysis of the FMR data with the assistance of M.B. M.A.

conducted the evaporation of all the Au/Co-based heterostructures. M.R. and R.C. conducted the growth of the Sb₂Te₃ layers under the supervision of M.L. C.W. contributed to the XRR data analysis. L.L. did the MC and R measurements. P.T. and A.D. performed ARPES. G.G. conducted BLS on selected samples. M.F. supervised the FMR measurements. R.M. conceived the experiments and coordinated the research activity. E.L. and R.M. wrote the manuscript. All authors discussed the results and reviewed the manuscript and the Supporting Information.

Data Availability Statement

The data that support the findings of this study are available from the corresponding author upon reasonable request.

Keywords

Edelstein effect, ferromagnetic resonance, metal-organic chemical vapor deposition, spin pumping, spintronics, two-magnon scattering

Received: September 16, 2021

Published online: October 15, 2021

- [1] M. Z. Hasan, C. L. Kane, *Rev. Mod. Phys.* **2010**, *82*, 3045.
- [2] A. Hirohata, K. Yamada, Y. Nakatani, L. Prejbeanu, B. Diény, P. Pirro, B. Hillebrands, *J. Magn. Magn. Mater.* **2020**, *509*, 166711.
- [3] J. Ryu, S. Lee, K. J. Lee, B. G. Park, *Adv. Mater.* **2020**, *32*, 1907148.
- [4] J. Puebla, J. Kim, K. Kondou, Y. Otani, *Commun. Mater.* **2020**, *1*, 24.
- [5] J. Sinova, S. O. Valenzuela, J. Wunderlich, C. H. Back, T. Jungwirth, *Rev. Mod. Phys.* **2015**, *87*, 1213.
- [6] A. Soumyanarayanan, N. Reyren, A. Fert, C. Panagopoulos, **2016**, *539*, 509.
- [7] Y. Otani, M. Shiraishi, A. Oiwa, E. Saitoh, S. Murakami, *Nat. Phys.* **2017**, *13*, 829.
- [8] X. Wang, L. Cheng, D. Zhu, Y. Wu, M. Chen, Y. Wang, D. Zhao, C. B. Boothroyd, Y. M. Lam, J. X. Zhu, M. Battiato, J. C. W. Song, H. Yang, E. E. M. Chia, *Adv. Mater.* **2018**, *30*, 1802356.
- [9] H. Zhang, C. X. Liu, X. L. Qi, X. Dai, Z. Fang, S. C. Zhang, *Nat. Phys.* **2009**, *5*, 438.
- [10] Y. L. Chen, J. G. Analytis, J. H. Chu, Z. K. Liu, S. K. Mo, X. L. Qi, H. J. Zhang, P. H. Lu, X. Dai, Z. Fang, S. C. Zhang, I. R. Fisher, Z. Hussain, Z. X. Shen, *Science* **2009**, *325*, 178.
- [11] Y. Xia, D. Qian, D. Hsieh, L. Wray, A. Pal, H. Lin, A. Bansil, D. Grauer, Y. S. Hor, R. J. Cava, M. Z. Hasan, *Nat. Phys.* **2009**, *5*, 398.
- [12] A. R. Mellnik, J. S. Lee, A. Richardella, J. L. Grab, P. J. Mintun, M. H. Fischer, A. Vaezi, A. Manchon, E. A. Kim, N. Samarth, D. C. Ralph, *Nature* **2014**, *511*, 449.
- [13] L. A. Walsh, C. M. Smyth, A. T. Barton, Q. Wang, Z. Che, R. Yue, J. Kim, M. J. Kim, R. M. Wallace, C. L. Hinkle, *J. Phys. Chem. C* **2017**, *121*, 23551.
- [14] H. Wu, P. Zhang, P. Deng, Q. Lan, Q. Pan, S. A. Razavi, X. Che, L. Huang, B. Dai, K. Wong, X. Han, K. L. Wang, *Phys. Rev. Lett.* **2019**, *123*, 207205.
- [15] N. Peranio, M. Winkler, D. Bessas, Z. Aabdin, J. König, H. Böttner, R. P. Hermann, O. Eibl, *J. Alloys Compd.* **2012**, *521*, 163.
- [16] Y. Wang, D. Zhu, Y. Wu, Y. Yang, J. Yu, R. Ramaswamy, R. Mishra, S. Shi, M. Elyasi, K. L. Teo, Y. Wu, H. Yang, *Nat. Commun.* **2017**, *8*, 1364.
- [17] M. Dc, T. Liu, J. Y. Chen, T. Peterson, P. Sahu, H. Li, Z. Zhao, M. Wu, J. P. Wang, *Appl. Phys. Lett.* **2019**, *114*, 102401.
- [18] R. Ramaswamy, T. Dutta, S. Liang, G. Yang, M. S. M. Saifullah, H. Yang, *J. Phys. D: Appl. Phys.* **2019**, *52*, 224001.
- [19] W. J. Wang, K. H. Gao, Z. Q. Li, *Sci. Rep.* **2016**, *6*, 25291.
- [20] E. Longo, R. Mantovan, R. Cecchini, M. D. Overbeek, M. Longo, G. Trevisi, L. Lazzarini, G. Tallarida, M. Fanciulli, C. H. Winter, C. Wiemer, *Nano Res.* **2020**, *13*, 570.
- [21] M. Rimoldi, R. Cecchini, C. Wiemer, A. Lamperti, E. Longo, L. Nasi, L. Lazzarini, R. Mantovan, M. Longo, *RSC Adv.* **2020**, *10*, 19936.
- [22] A. Zavabeti, A. Jannat, L. Zhong, A. A. Haidry, Z. Yao, J. Z. Ou, *Nano-Micro Lett.* **2020**, *12*, 66.
- [23] R. Cecchini, R. Mantovan, C. Wiemer, L. Nasi, L. Lazzarini, M. Longo, *Phys. Status Solidi RRL* **2018**, *12*, 1800155.
- [24] Y. Tserkovnyak, A. Brataas, G. E. W. Bauer, *Phys. Rev. B: Condens. Matter Mater. Phys.* **2002**, *66*, 224403.
- [25] Y. Tserkovnyak, A. Brataas, G. E. W. Bauer, *Phys. Rev. Lett.* **2002**, *88*, 4.
- [26] J. C. Rojas-Sánchez, S. Oyarzún, Y. Fu, A. Marty, C. Vergnaud, S. Gambarelli, L. Vila, M. Jamet, Y. Ohtsubo, A. Taleb-Ibrahimi, P. Le Fèvre, F. Bertran, N. Reyren, J. M. George, A. Fert, *Phys. Rev. Lett.* **2016**, *116*, 096602.
- [27] J. B. S. Mendes, A. Aparecido-Ferreira, J. Holanda, A. Azevedo, S. M. Rezende, *Appl. Phys. Lett.* **2018**, *112*, 242407.
- [28] M. Jamali, J. S. Lee, J. S. Jeong, F. Mahfouzi, Y. Lv, Z. Zhao, B. K. Nikolić, K. A. Mkhoyan, N. Samarth, J. P. Wang, *Nano Lett.* **2015**, *15*, 7126.
- [29] B. L. Zink, M. Manno, L. O'Brien, J. Lotze, M. Weiler, D. Bassett, S. J. Mason, S. T. B. Goennenwein, M. Johnson, C. Leighton, *Phys. Rev. B* **2016**, *93*, 184401.
- [30] S. Mizukami, Y. Ando, T. Miyazaki, *Jpn. J. Appl. Phys., Part 1* **2001**, *40*, 580.
- [31] J. C. R. Sánchez, L. Vila, G. Desfonds, S. Gambarelli, J. P. Attané, J. M. De Teresa, C. Magén, A. Fert, *Nat. Commun.* **2013**, *4*, 2944.
- [32] M. Dc, J. Y. Chen, T. Peterson, P. Sahu, B. Ma, N. Mousavi, R. Harjani, J. P. Wang, *Nano Lett.* **2019**, *19*, 4836.
- [33] V. M. Edelstein, *Solid State Commun.* **1990**, *73*, 233.
- [34] P. Deorani, J. Son, K. Banerjee, N. Koirala, M. Brahlek, S. Oh, H. Yang, *Phys. Rev. B: Condens. Matter Mater. Phys.* **2014**, *90*, 94403.
- [35] C. Pauly, G. Bihlmayer, M. Liebmann, M. Grob, A. Georgi, D. Subramaniam, M. R. Scholz, J. Sánchez-Barriga, A. Varykhalov, S. Blügel, O. Rader, M. Morgenstern, *Phys. Rev. B: Condens. Matter Mater. Phys.* **2012**, *86*, 235106.
- [36] G. Bendt, S. Zastrow, K. Nielsch, P. S. Mandal, J. Sánchez-Barriga, O. Rader, S. Schulz, *J. Mater. Chem. A* **2014**, *2*, 8215.
- [37] C. Z. Chang, P. Tang, X. Feng, K. Li, X. C. Ma, W. Duan, K. He, Q. K. Xue, *Phys. Rev. Lett.* **2015**, *115*, 136801.
- [38] A. Ghosh, J. F. Sierra, S. Auffret, U. Ebels, W. E. Bailey, *Appl. Phys. Lett.* **2011**, *98*, 052508.
- [39] M. Tokaç, S. A. Bunyaev, G. N. Kakazei, D. S. Schmool, D. Atkinson, A. T. Hindmarch, *Phys. Rev. Lett.* **2015**, *115*, 056601.
- [40] M. Farle, *Rep. Prog. Phys.* **1998**, *61*, 755.
- [41] Y. Tserkovnyak, A. Brataas, G. E. W. Bauer, B. I. Halperin, *Rev. Mod. Phys.* **2005**, *77*, 1375.
- [42] L. Zhu, D. C. Ralph, R. A. Buhrman, *Phys. Rev. Lett.* **2019**, *123*, 57203.
- [43] K. Chen, S. Zhang, *Phys. Rev. Lett.* **2015**, *114*, 126602.
- [44] B. Heinrich, J. F. Cochran, R. Hasegawa, *J. Appl. Phys.* **1985**, *57*, 3690.
- [45] T. G. A. Verhagen, H. N. Tinkley, H. C. Overweg, M. Van Son, M. Huber, J. M. Van Ruitenbeek, J. Aarts, *J. Phys.: Condens. Matter* **2016**, *28*, 056004.
- [46] M. J. Hurben, C. E. Patton, *J. Appl. Phys.* **1998**, *83*, 4344.
- [47] J. Lindner, I. Barsukov, C. Raeder, C. Hassel, O. Posth, R. Meckenstock, P. Landeros, D. L. Mills, *Phys. Rev. B: Condens. Matter Mater. Phys.* **2009**, *80*, 224421.
- [48] S. Jiang, L. Sun, Y. Yin, Y. Fu, C. Luo, Y. Zhai, H. Zhai, *AIP Adv.* **2017**, *7*, 056029.
- [49] A. Azevedo, A. B. Oliveira, F. M. de Aguiar, S. M. Rezende, *Phys. Rev. B* **2000**, *62*, 5331.

- [50] Y. Cheng, A. J. Lee, J. T. Brangham, S. P. White, W. T. Ruane, P. C. Hammel, F. Yang, *Appl. Phys. Lett.* **2018**, *113*, 262403.
- [51] J. Dubowik, K. Załęski, H. Głowiński, I. Gociańska, *Phys. Rev. B: Condens. Matter Mater. Phys.* **2011**, *84*, 184438.
- [52] J. Bass, W. P. Pratt, *J. Phys.: Condens. Matter* **2007**, *19*, 183201.
- [53] A. K. Kaveev, A. G. Banskchikov, A. N. Terpitskiy, V. A. Golyashov, O. E. Tereshchenko, K. A. Kokh, D. A. Estyunin, A. M. Shikin, *Semiconductors* **2020**, *54*, 1051.
- [54] Y. Wang, R. Ramaswamy, H. Yang, *J. Phys. D: Appl. Phys.* **2018**, *51*, 273002.
- [55] K. Kondou, R. Yoshimi, A. Tsukazaki, Y. Fukuma, J. Matsuno, K. S. Takahashi, M. Kawasaki, Y. Tokura, Y. Otani, *Nat. Phys.* **2016**, *12*, 1027.
- [56] A. A. Baker, A. I. Figueroa, L. J. Collins-Mcintyre, G. Van Der Laan, T. Hesjedal, *Sci. Rep.* **2015**, *5*, 7907.
- [57] A. Ruiz-Calaforra, T. Brächer, V. Lauer, P. Pirro, B. Heinz, M. Geilen, A. V. Chumak, A. Conca, B. Leven, B. Hillebrands, *J. Appl. Phys.* **2015**, *117*, 163901.
- [58] O. Mosendz, J. E. Pearson, F. Y. Fradin, G. E. W. Bauer, S. D. Bader, A. Hoffmann, *Phys. Rev. Lett.* **2010**, *104*, 046601.
- [59] K. Ando, S. Takahashi, J. Ieda, Y. Kajiwara, H. Nakayama, T. Yoshino, K. Harii, Y. Fujikawa, M. Matsuo, S. Maekawa, E. Saitoh, *J. Appl. Phys.* **2011**, *109*, 103913.
- [60] A. Azevedo, L. H. Vilela-Leão, R. L. Rodríguez-Suárez, A. F. Lacerda Santos, S. M. Rezende, *Phys. Rev. B: Condens. Matter Mater. Phys.* **2011**, *83*, 144402.
- [61] M. Harder, Z. X. Cao, Y. S. Gui, X. L. Fan, C. M. Hu, *Phys. Rev. B: Condens. Matter Mater. Phys.* **2011**, *84*, 054423.
- [62] E. Saitoh, M. Ueda, H. Miyajima, G. Tatara, *Appl. Phys. Lett.* **2006**, *88*, 182509.
- [63] K. I. Uchida, H. Adachi, T. Ota, H. Nakayama, S. Maekawa, E. Saitoh, *Appl. Phys. Lett.* **2010**, *97*, 172505.
- [64] F. Bonell, M. Goto, G. Sauthier, J. F. Sierra, A. I. Figueroa, M. V. Costache, S. Miwa, Y. Suzuki, S. O. Valenzuela, *Nano Lett.* **2020**, *20*, 5893.
- [65] C. T. Boone, H. T. Nembach, J. M. Shaw, T. J. Silva, *J. Appl. Phys.* **2013**, *113*, 153906.
- [66] Y. Wang, P. Deorani, K. Banerjee, N. Koirala, M. Brahlek, S. Oh, H. Yang, *Phys. Rev. Lett.* **2015**, *114*, 257202.
- [67] G. Zahnd, L. Vila, V. T. Pham, M. Cosset-Cheneau, W. Lim, A. Brenac, P. Laczkowski, A. Marty, J. P. Attané, *Phys. Rev. B* **2018**, *98*, 174414.
- [68] J. Sinova, D. Culcer, Q. Niu, N. A. Sinitsyn, T. Jungwirth, A. H. MacDonald, *Phys. Rev. Lett.* **2004**, *92*, 126603.
- [69] J. B. S. Mendes, O. Alves Santos, J. Holanda, R. P. Loreto, C. I. L. De Araujo, C. Z. Chang, J. S. Moodera, A. Azevedo, S. M. Rezende, *Phys. Rev. B* **2017**, *96*, 180415.
- [70] Z. Feng, J. Hu, L. Sun, B. You, D. Wu, J. Du, W. Zhang, A. Hu, Y. Yang, D. M. Tang, B. S. Zhang, H. F. Ding, *Phys. Rev. B: Condens. Matter Mater. Phys.* **2012**, *85*, 214423.
- [71] Y. Shiomi, K. T. Yamamoto, R. Nakanishi, T. Nakamura, S. Ichinokura, R. Akiyama, S. Hasegawa, E. Saitoh, *Appl. Phys. Lett.* **2018**, *113*, 052401.
- [72] E. Longo, C. Wiemer, M. Belli, R. Cecchini, M. Longo, M. Cantoni, C. Rinaldi, M. D. Overbeek, C. H. Winter, G. Gubbiotti, G. Tallarida, M. Fanciulli, R. Mantovan, *J. Magn. Magn. Mater.* **2020**, *509*, 166885.
- [73] K. Nakahashi, K. Takaishi, T. Suzuki, K. Kanemoto, *ACS Appl. Electron. Mater.* **2021**, *3*, 1663.
- [74] R. Sun, S. Yang, X. Yang, A. Kumar, E. Vetter, W. Xue, Y. Li, N. Li, Y. Li, S. Zhang, B. Ge, X. Zhang, W. He, A. F. Kemper, D. Sun, Z. Cheng, *Adv. Mater.* **2020**, *32*, 2005315.
- [75] V. Vlaminck, J. E. Pearson, S. D. Bader, A. Hoffmann, *Phys. Rev. B: Condens. Matter Mater. Phys.* **2013**, *88*, 064414.
- [76] W. Zhang, W. Han, X. Jiang, S. H. Yang, S. S. P. Parkin, *Nat. Phys.* **2015**, *11*, 496.
- [77] K. T. Yamamoto, Y. Shiomi, K. Segawa, Y. Ando, E. Saitoh, *Phys. Rev. B* **2016**, *94*, 024404.
- [78] P. Noel, C. Thomas, Y. Fu, L. Vila, B. Haas, P. H. Jouneau, S. Gambarelli, T. Meunier, P. Ballet, J. P. Attané, *Phys. Rev. Lett.* **2018**, *120*, 167201.
- [79] H. Wang, J. Kally, J. S. Lee, T. Liu, H. Chang, D. R. Hickey, K. A. Mkhoyan, M. Wu, A. Richardella, N. Samarth, *Phys. Rev. Lett.* **2016**, *117*, 076601.
- [80] R. Sun, S. Yang, X. Yang, E. Vetter, D. Sun, N. Li, L. Su, Y. Li, Y. Li, Z. Z. Gong, Z. K. Xie, K. Y. Hou, Q. Gul, W. He, X. Q. Zhang, Z. H. Cheng, *Nano Lett.* **2019**, *19*, 4420.
- [81] J. Ding, C. Liu, Y. Zhang, V. Kalappattil, R. Yu, U. Erugu, J. Tang, H. Ding, H. Chen, M. Wu, *Adv. Funct. Mater.* **2021**, *31*, 2008411.
- [82] S. Manipatruni, D. E. Nikonov, C. C. Lin, T. A. Gosavi, H. Liu, B. Prasad, Y. L. Huang, E. Bonturim, R. Ramesh, I. A. Young, *Nature* **2019**, *565*, 35.
- [83] J. B. S. Mendes, M. Gamino, R. O. Cunha, J. E. Abrao, S. M. Rezende, A. Azevedo, *Phys. Rev. Mater.* **2021**, *5*, 024206.
- [84] E. Longo, C. Wiemer, R. Cecchini, M. Longo, A. Lamperti, A. Khanas, A. Zenkevich, M. Fanciulli, R. Mantovan, *J. Magn. Magn. Mater.* **2019**, *474*, 632.
- [85] E. Longo, C. Wiemer, R. Cecchini, M. Longo, A. Lamperti, A. Khanas, A. Zenkevich, M. Cantoni, C. Rinaldi, M. Fanciulli, R. Mantovan, *Adv. Mater. Interfaces* **2020**, *7*, 2000905.
- [86] Y. Jiang, Y. Wang, M. Chen, Z. Li, C. Song, K. He, L. Wang, X. Chen, X. Ma, Q. K. Xue, *Phys. Rev. Lett.* **2012**, *108*, 2.
- [87] S. Zhang, A. Fert, *Phys. Rev. B* **2016**, *94*, 184423.
- [88] S. H. Su, P.-Y. Chuang, J.-C. Lee, C.-W. Chong, Y. W. Li, Z. M. Lin, Y.-C. Chen, C.-M. Cheng, J.-C.-A. Huang, *ACS Appl. Electron. Mater.* **2021**, *3*, 2988.
- [89] S. Tacchi, M. Madami, G. Gubbiotti, G. Carlotti, A. O. Adeyeye, S. Neusser, B. Botters, D. Grundler, *IEEE Trans. Magn.* **2010**, *46*, 172.